Chinese Chemical Letters 34 (2023) 107881

Contents lists available at ScienceDirect

Chinese Chemical Letters

journal homepage: www.elsevier.com/locate/cclet

Improving performance of ZnO Schottky photodetector by inserting MXenes modified-layer

Cheng Wu[a], Xinzhi Luo[b], Xiaoming Yu[a,b,*], Xuan Yu[a,b,*], Kun Lin[a], Minghao Li[a], Zhenhua Li[a], Yu Cao[c], Yingtang Zhou[b,*]

[a] School of Marine Engineering Equipment, Zhejiang Ocean University, Zhoushan 316022, China
[b] National Engineering Research Center for Marine Aquaculture, Zhejiang Ocean University, Zhoushan 316022, China
[c] School of Electrical Engineering, Northeast Electric Power University, Jilin 132012, China

ARTICLE INFO

Article history:
Received 18 July 2022
Revised 11 August 2022
Accepted 4 October 2022
Available online 12 October 2022

Keywords:
MXenes
$Ti_3C_2T_X$
Schottky
Photodetector
Responsivity
Normalized detectivity

ABSTRACT

The development of low-cost and high-performance ZnO Schottky photodetectors (PDs) has drawn intensive attention, but still a challenge due to their poor conductivity and low light utilization efficiency. Here, we introduce $Ti_3C_2T_X$ into ZnO films to fabricate Schottky UV PDs *via* facile spin-coated method. The fabricated ZnO/$Ti_3C_2T_X$/ZnO compound film shows outstanding performance on photocurrent, responsivity, noise equivalent power (NEP), normalized detection rate (D^*), and linear dynamic region (LDR), compared with the original ZnO device. The photocurrent is significantly increased by 466%, and the responsivity is improved by one order of magnitude. In addition, it exhibits relatively low NEP (5.99×10^{-11} W), strong D^* (2.53×10^9 Jones), and high LDR (28 dB). The superior performance is ascribed to the enhanced conductivity and light absorption of ZnO film after introduction of $Ti_3C_2T_X$ modification layer, leading to simultaneously faster electron transfer, lower the radiation recombination of electron and holes on the ZnO/$Ti_3C_2T_X$/ZnO compound film. This work provides a facile way to develop low-cost and high-performance ZnO Schottky PDs.

© 2023 Published by Elsevier B.V. on behalf of Chinese Chemical Society and Institute of Materia Medica, Chinese Academy of Medical Sciences.

As an electronic device that uses electrical signals to perceive optical signals, photodetectors (PDs) are widely used in various fields such as missile launch detection, visual communications, and flame monitoring [1–6]. Schottky junction PDs have attracted much attention due to their simple structure, good responsivity, and response time [7]. The PDs of this structure formed by depositing a metal electrode (~4.2 eV to 6.32 eV) with a significant work function on the surface of a semiconductor (such as an n-type semiconductor) [8]. Tsai *et al.* prepared metal-semiconductor-metal (MSM) Schottky UV PDs based on $ZnGa_2O_4$ thin film in 2019 [9]; Wang *et al.* prepared flexible UV PDs based on ZnO/Ag Schottky junction [10]. Schottky PDs consists of GaAs/TiO_2 obtained good performance [11,12]. Due to wide direct bandgap (~3.37 eV), the high exciton binding energy (60 meV), especially the low-cost solution-processed ZnO, is widely used in the ultraviolet Schottky PDs [13–16]. However, solution-prepared ZnO films have poor conductivity and more defects, which limit the migration of carriers and the light utilization [13,17]. It is important to improvement ZnO thin-films with superior electron transport properties for PDs. Doping elements is a good way to improve the conductivity of ZnO, such as Al-doped ZnO [18] and Ag NWs-doped ZnO [19,20].

Recently, a new family of novel two-dimensional transition metal carbides, nitrides, and carbonitrides (MXenes) has emerged, which has attracted extensive attention due to their unique physical and chemical properties [21–23]. MXenes consists of $M_{n+1}X_nT_X$, where M represents an early transition metal (Ti, Nb, Mo, *etc.*), X represents C or N, and T represents a surface functional group (-OH, -O-, or -F) [21,23–25]. This novel material is obtained by selectively etching away the A layer atoms (A is Al or Si element, *etc.*) in the MAX phase and replacing the M-A metal bond in the $M_{n+1}AX_n$ phase with OH, O or F [24,26] (Fig. 1a). As a representative member of the MXenes group, $Ti_3C_2T_X$ has been used in optoelectronic devices due to its excellent conductivity, hydrophilicity, high transmittance and electron mobility [11,24,27,28]. $Ti_3C_2T_X$ nanosheets have two exposed Ti atoms, and the octahedral positions of Ti-atoms are filled with C-atoms. It became an attractive material for optoelectronic devices since was first explored in 2011 [11]. Guo *et al.* added 0.03 wt% $Ti_3C_2T_X$ powder into the perovskite layer and the PCE of PSCs improved by 12% [26]; Hou and Yu added

* Corresponding authors at: National Engineering Research Center for Marine Aquaculture, Zhejiang Ocean University, Zhoushan 316022, China.
E-mail addresses: yuxm@zjou.edu.cn (X. Yu), yuxuan@zjou.edu.cn (X. Yu), zhouyingtang@zjou.edu.cn (Y. Zhou).

https://doi.org/10.1016/j.cclet.2022.107881
1001-8417/© 2023 Published by Elsevier B.V. on behalf of Chinese Chemical Society and Institute of Materia Medica, Chinese Academy of Medical Sciences.

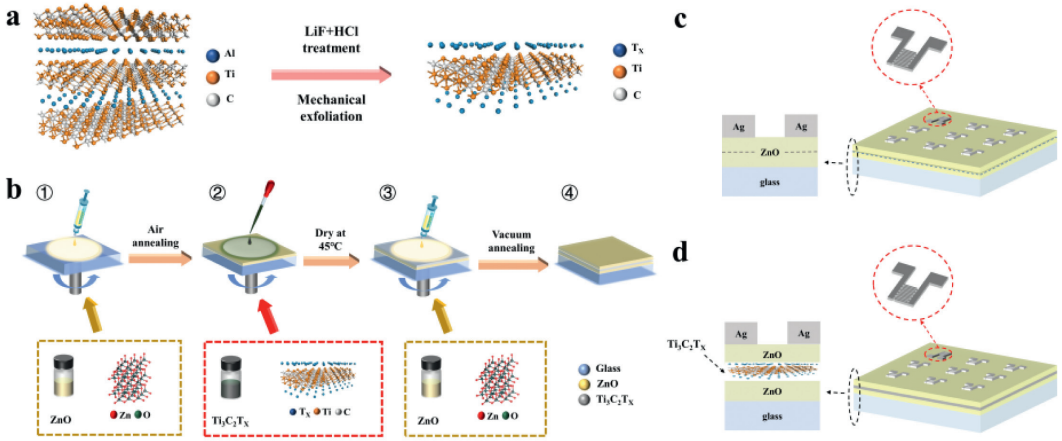

Fig. 1. (a) Preparation process of $Ti_3C_2T_X$ nanosheets. (b) Preparation process. (c) Schematic diagram of ZnO device. (d) Schematic diagram of $Ti_3C_2T_X$ modified device.

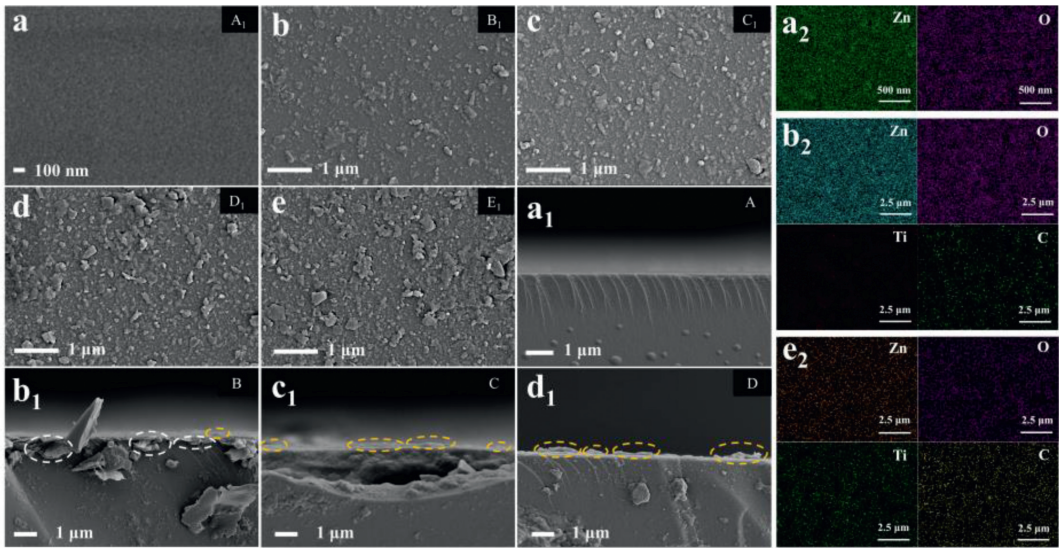

Fig. 2. (a–e) SEM top view of samples A_1-E_1 (the number of $Ti_3C_2T_X$ layers in the ZnO/$Ti_3C_2T_X$ composite films increased from 0 to 1, 2, 3 and 4, named as samples A_1, B_1, C_1, D_1 and E_1). (a_1-d_1) SEM cross-sectional views of samples A-D ($Ti_3C_2T_X$: 0-3 layers). (a_2, b_2, e_2) EDS mapping images of samples A ($Ti_3C_2T_X$-0), B ($Ti_3C_2T_X$-1) and E ($Ti_3C_2T_X$-4).

$Ti_3C_2T_X$ powder into ZnO sol-gel solution can improve the conductivity and passivated surface, thus improving the performance of inverted polymer solar cells [24]. In addition, $Ti_3C_2T_X$ exhibits a local surface plasmon resonance (LSPR) under the irradiation of incident light, showing intensive absorption [29–31].

Inspired by these works, we first investigated the effect of inserting $Ti_3C_2T_X$ nanosheets into ZnO thin films on the performance of ZnO Schottky PDs. In this work, we fabricated a Schottky junction PDs of Glass/ZnO/$Ti_3C_2T_X$-X (X from 0 to 4)/ZnO/Ag by inserting $Ti_3C_2T_X$ layers between ZnO films (the fabrication process is shown in Figs. 1b–d are schematic diagrams of the device). By adjusting the content of $Ti_3C_2T_X$, and study the effect of $Ti_3C_2T_X$ on the performance of ZnO Schottky PDs, we found that $Ti_3C_2T_X$ improves the optical utilization and electrical properties of ZnO, resulting in an enhanced photocurrent (from 0.44 μA to 14.51 μA), normalized detectivity (D*), and responsivity (R_S, from 1.92×10^{-3} A/W to 6.17×10^{-2} A/W). This study provides guidance for the development of high-performance ZnO Schottky PDs.

Firstly, SEM views of the samples with and without $Ti_3C_2T_X$ modified layer are shown in Figs. 2a–e. One can see that the distribution of $Ti_3C_2T_X$ nanosheets becomes denser with increasing the content of $Ti_3C_2T_X$, and nanosheets stacking is more likely to occur. Cross-sectional view of the samples A-D can be seen in Figs. 2a_1-d_1. Where the white circles indicate that the $Ti_3C_2T_X$ nanosheets were successfully intercalated in ZnO films, and the formed composite films had small bulges (yellow circles) on the surface, which increased the surface roughness of the composite films. Element mapping were tested to further demonstrate the successful fabrication of the ZnO/$Ti_3C_2T_X$/ZnO thin film, and the results are shown in Figs. 2a_2, b_2, and e_2. The colorful images show the distributions of Zn, O, Ti, and C elements, which are uniformly distributed. Fig. 2b_2 shows the element mappings after inserting a layer of $Ti_3C_2T_X$ (sample B), the Ti and C elements are obviously emerged, indicating the successful insertion of $Ti_3C_2T_X$ nanosheets compared with ZnO thin-film (sample A, Fig. 2a_2). Fig. 2e_2 shows the element mappings after inserting 4 layers of $Ti_3C_2T_X$ (sample E), there are more bright spots clustered together in the Ti and C element distribution map of device E, indicating that the $Ti_3C_2T_X$ nanosheets are more prone to packing with the increase of $Ti_3C_2T_X$ content.

The atomic force microscopy (AFM) was used to further study the influence of the stacking on the surface morphology of the film, as shown in Figs. S1a–f (Supporting information). Thin-films A: $Ti_3C_2T_X$-0, B: $Ti_3C_2T_X$-1, and E: $Ti_3C_2T_X$-4 were selected as representatives. Obviously, the ZnO film without $Ti_3C_2T_X$ modified layer (A, Figs. S1a and d) has more even surface, the nanoparticles are finely dispersed and more uniform, and the wrinkles are rel-

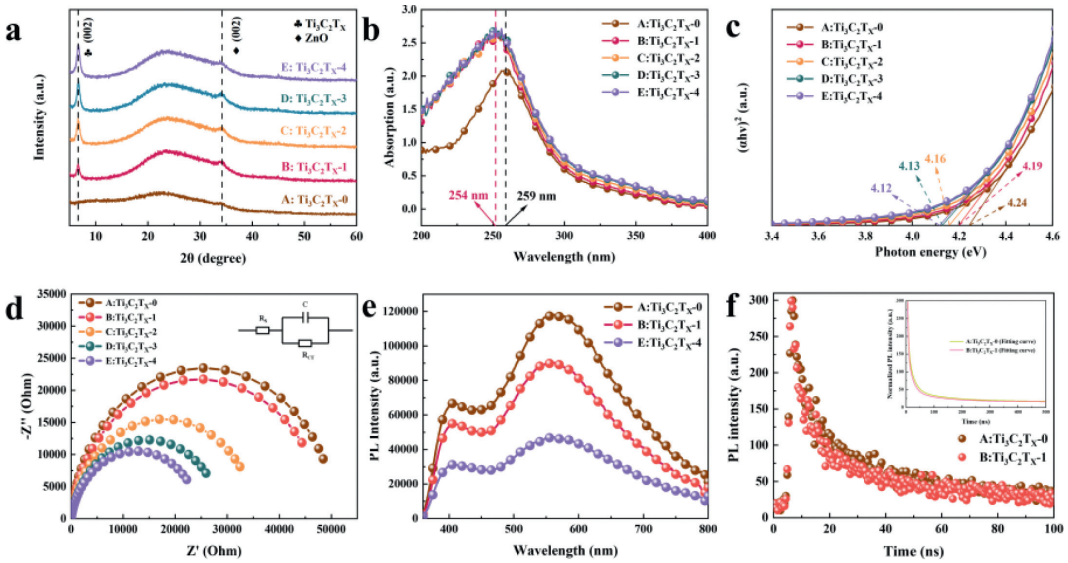

Fig. 3. (a) XRD patterns of samples with different $Ti_3C_2T_X$ layers. (b) Absorption curves of samples A-E at 200–400 nm. (c) $(ahv)^2$ – hv function curve obtained from absorption. (d) Nyquist plot (fitted curve) and equivalent circuit diagram of samples with different $Ti_3C_2T_X$ layers. (e) PL and (f) TRPL spectra of ZnO/$Ti_3C_2T_X$/ZnO films on glass substrates.

atively shallow. Specifically, the addition of $Ti_3C_2T_X$ increases the surface roughness of the film. In general, the films with appropriate surface roughness have better micro-morphology and appropriate domain size, can increase the contact area with electrode [24]. However, the charge recombination centers will increase with increasing root-mean-square (RMS) roughness of thin films, leading to the trap-assisted recombination [24].

XRD results of the ZnO/$Ti_3C_2T_X$/ZnO composite films are shown in Fig. 3a. The (002) diffraction peak of hexagonal wurtzite ZnO appeared at about 34.4° of all five samples. The films with $Ti_3C_2T_X$ intercalation show higher ZnO (002) diffraction peaks, indicating that the addition of $Ti_3C_2T_X$ promotes the crystallization of ZnO. In addition, samples B, C, D and E all showed (002) diffraction peaks representing $Ti_3C_2T_X$ at around 6.6°, and the intensity of the characteristic peaks increased with the increase of the $Ti_3C_2T_X$ layers (Fig. S2a in Supporting information). The total-transmittance (T_{total}) and spectral-transmittance ($T_{spectral}$) of the ZnO/$Ti_3C_2T_X$-X/ZnO composite thin films as shown in Figs. S2c and d (Supporting information). Compared with ZnO films, the composite films with $Ti_3C_2T_X$ exhibited relatively lower transmittance from 300 nm to 800 nm. Which can be attributed to the unique optical properties of $Ti_3C_2T_X$ [24].

The UV absorption can be seen in Fig. 3b. The absorption peak of ZnO located at 259 nm, which slightly blue-shifted (254 nm) after inserting the $Ti_3C_2T_X$ (Fig. S2b in Supporting information). With the increase of $Ti_3C_2T_X$ content, the absorption intensity increased. The absorption of composite film is correspondingly improved due to the strong light limitation of LSPR [3,29,32]. We calculated the optical bandgap of the film from absorption curve by the Tauc formula:

$$(ahv)^{1/n} = A(hv - E_g) \quad (1)$$

where α is the absorbance index, h is Planck's constant, v is the frequency, A is a constant, and E_g is the bandgap of the semiconductor. With the increase of $Ti_3C_2T_X$ layer, the optical bandgap decreased from 4.24 eV (sample A) to 4.12 eV (Sample E) due to the strong electronegativity mismatch between atoms and the appearance of impurity level in the bandgap of ZnO (Fig. 3c) [3,33]. It shows that $Ti_3C_2T_X$ can improve the light absorption and enhance the light utilization rate.

We characterized the device's conductivity by using electrochemical impedance spectroscopy (EIS). The equivalent circuit consisting of series resistance (R_S), charge transfer resistance (R_{ct}), and parallel capacitance (C) are shown in the inset of Fig. 3d. The R_{ct} decreased from around 50,000 (sample A) to approximately 23,000 (sample E), demonstrating the increased conductivity of the composite films. The high conductivity and electron mobility of the $Ti_3C_2T_X$ modified ZnO composite thin films can be beneficial to reducing the R_{ct} and increasing the charge transfer efficiency, thereby improving the device performance [26].

Fig. 3e depicts the steady-state PL fluorescence spectrum. There are mainly two emission bands of ZnO films, in which the near-band-edge emission (NBE) at around 405 nm is attributed to the quenching ability of photogenerated excitons, while the broad visible emission defect emission peak (DLE) originates from the defects [24,34]. It can be seen that the NBE peak appeared around 405 nm rather than around 370 nm (Stoke shift), which can be induced by the accelerated formation of interstitial zinc at relatively higher temperature [33,35]. Zinc interstitials, as well as charge transfer between deep levels and oxygen dangling bonds are the most commonly reported defects for the defect emission [24,36,37]. The broadband defect emission obviously suppressed after the interposition, indicating that the defects in the ZnO/$Ti_3C_2T_X$/ZnO film reduced. In addition, the intensity ratio of NBE peak to DLE calculated by Gaussian model is also an important factor, which is usually proportional to the crystallization characteristics of ZnO particles caused by defect passivation [24,38]. The NBE/DLE intensity ratio is 0.56 (sample A), 0.61 and 0.66, respectively for sample B and sample E, as shown in Table S2 (Supporting information). It can be found that the NBE/DLE ratio is slightly higher than that of the ZnO sample, indicating that the insertion of $Ti_3C_2T_X$ layer is helpful to improve the crystallization characteristics of ZnO particles, which is consistent with the XRD results.

The time-resolved photoluminescence (TRPL) spectra used to further investigate the effect of the $Ti_3C_2T_X$ insertion layer on the exciton dynamics and charge transport of the device. TRPL decay curves were fitted by the double exponential function: $I(t) = I(0) \times [A_1 \exp(-t/\tau_1) + A_2 \exp(-t/\tau_2)]$, and the average lifetime of TRPL is calculated by formula: $\tau_{ave} = (A_1\tau_1^2 + A_2\tau_2^2)/(A_1\tau_1 + A_2\tau_2)$ [39,40]. Here, films A: $Ti_3C_2T_X$-0 and B: $Ti_3C_2T_X$-1 was selected as representatives (Fig. 3f, inset is the TRPL spectrum after fitting).

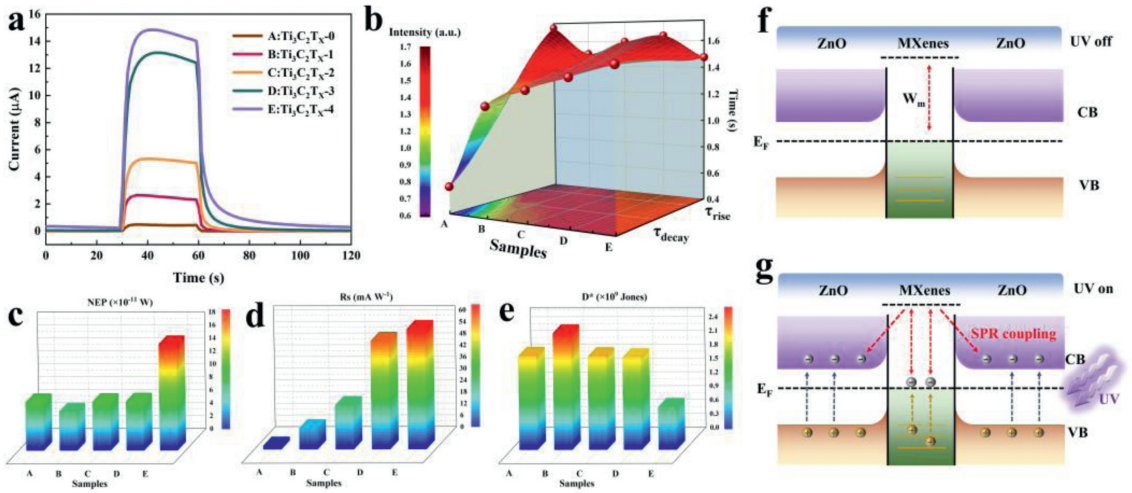

Fig. 4. (a) Temporal photoresponse of the device at 5 V bias voltage under 360 nm illumination (10 mW/cm^2). (b) Rise-decay time (τ) curves of samples with different $Ti_3C_2T_X$ layers. (c-e) Noise equivalent power (NEP), responsivity (R_S), and normalized detectability (D^*) of samples with different $Ti_3C_2T_X$ layers. (f, g) Schematics of the energy band diagrams of the photodetector and the charge transfer process under UV illumination.

Meanwhile, the relevant data for TRPL are demonstrated in Table S3 (Supporting information). τ_1 correlates with radiative recombination of free charge carriers due to traps, which means the recombination before free charge carriers are extracted by the thin film [40]. τ_2 of the sample B ($Ti_3C_2T_X$-1) shows the least time, indicating that this thin film effectively extracts electrons due to the high mobility [24,40]. Moreover, the normalized TRPL shows a faster decay ($\tau_{ave} = 60.52$ ns) of sample B ($Ti_3C_2T_X$-1) than that of sample A ($Ti_3C_2T_X$-0, $\tau_{ave} = 70.03$ ns). The shorter lifetime shown by the ZnO/$Ti_3C_2T_X$/ZnO sample compared with the control sample are attributed to a faster extraction of charge carriers due to the presence of $Ti_3C_2T_X$, and this is consistent with the PL result [24,39,41,42]. However, the relatively lower PL life-time (sample B) also indicates that $Ti_3C_2T_X$ modified layer increases the non-radiative recombination formed by means other than photon radiation [39,42-44].

The effects of $Ti_3C_2T_X$ modified layers with different layers on the performance of ZnO/$Ti_3C_2T_X$/ZnO UV PDs were systematically investigated as shown in Fig. S3 (Supporting information). As shown in Fig. S3a, the ZnO/$Ti_3C_2T_X$/ZnO UV PDs shows a relatively higher I_d than the pristine PD at -10 V to 10 V bias due to the introduction of the $Ti_3C_2T_X$ modification layer, and I_d gradually increases with the increase of the number of $Ti_3C_2T_X$ layers, which may be due to the enhanced conductivity of the composite film. At the same time, compared with the original ZnO device, it is observed that I_{ph} of the ZnO/$Ti_3C_2T_X$/ZnO detector is significantly improved under 360 nm illumination at each bias, and I_{ph} increases more significantly with the increase of the number of $Ti_3C_2T_X$ layers, as shown in Fig. S3b. I_d and I_{ph} values obtained at 5 V bias are given for reference (Table S4 in Supporting information).

Fig. 4a shows the photoresponse of the ZnO Schottky PDs under 10 mW/cm^2 illumination (360 nm) after 5 V bias voltage. Compared with the ZnO PDs (device A), the devices incorporating $Ti_3C_2T_X$ (devices B, C, D and E) showed a higher photocurrent (Table S1 in Supporting information). Which can be attributed to the higher electrical conductivity of the composite films, significantly reduced internal resistance-induced current loss, and fast electron-hole collection [45]. This is consistent with the result of EIS. Also, the LSPR effect has contribution to the photocurrent [32,46]. Fig. S4f (Supporting information) is the magnified view of dark current. It observed that the dark current increases from 6.36×10^{-5} μA to 0.319 μA, with the increase of $Ti_3C_2T_X$. The dark current of the $Ti_3C_2T_X$ device sequentially stronger than that of the ZnO device, which may be caused by thermionic emission and tunneling current [32,47]. In addition, the rise in the dark current may also be arise from the $Ti_3C_2T_X$ layer, resulting in increased conductivity of ZnO [3,48].

In addition, the response speed of the PDs under UV light was investigated, by the rise time (τ_{rise}, the period of the current increased to I_{ph}/e) and decay time (τ_{decay}, period of the current decreased to $I_{ph} \times (1-1/e)$). Compared with the ZnO devices (Fig. S4a in Supporting information), the devices with $Ti_3C_2T_X$ modified layer (Figs. S4b–e in Supporting information) all exhibited lower τ_{rise}, as shown in Fig. 4b and Table S1. While, with the increase of $Ti_3C_2T_X$ content, the τ_{decay} of the device gradually increased from the original 0.595 s (device A) to 1.467 s (device E). Under UV irradiation, the conductivity of the film is improved due to the insertion of $Ti_3C_2T_X$, and most of the photogenerated carriers are more effectively transferred to the silver electrode and shorter response time (rise time).

The potential mechanism related to the photocurrent enhancement of the UV PDs is discussed (Figs. 4f and g). The $Ti_3C_2T_X$ nanosheets induce the intraband and interband excitation of electrons, called hot carriers associated with the nonradiative plasmonic decay [31,32,49,50]. Excited surface plasmons in 2D transition metal nanosheets can be attenuated by creating electron-hole pairs with much larger energy than carriers near the Fermi energy [32,51]. Meanwhile, for the large-sized nanosheets, the LSPR effect can also be achieved by high forward scattering toward the ZnO interface, and additional electron-hole pairs may be generated in the ZnO bandgap [52,53]. Given that $Ti_3C_2T_X$ nanostructures (vacuum annealing at 380 °C) have a higher work function ~4.8 eV than ZnO (sol-gel method), the energy band alignment as Fig. 4f to match the Fermi level [54–56] under dark conditions. Upon UV light irradiation, the photons energy can be absorbed by ZnO to generate electron-hole pairs (Fig. 4g). In addition, due to the collective oscillation of electrons and the spontaneous transfer of "hot electrons" excited by two-dimensional transition metal nanosheets to the conduction band of ZnO, and the significantly reduced internal resistance after the insertion of $Ti_3C_2T_X$ nanosheets, further enhances the electron transfer and extraction, thus improving the photocurrent [3,32].

On/off ratio, responsivity (R_S), noise equivalent power (NEP), normalized detectability (D^*), and linear dynamic region (LDR) are

important parameters for evaluating PDs, which can be expressed by the following formulas [46,57]:

$$\text{On/Off} = (I_{\text{photo}} - I_{\text{dark}})/I_{\text{dark}} \quad (2)$$

$$R_S = (I_{\text{photo}} - I_{\text{dark}})/P_0A \quad (3)$$

$$\text{NEP} = i_{\text{noise}}/R_S \quad (4)$$

$$D^* = R_S A^{1/2}/i_{\text{noise}} = R_S A^{1/2}/(2qI_{\text{dark}})^{1/2} \quad (5)$$

$$\text{LDR} = 20\log(J^*_{\text{ph}}/J_{\text{d}}) \quad (6)$$

where I_{photo} and I_{dark} are the photocurrent and dark current of the PDs, P_0 is the incident light power of 10 mW/cm^2 at 360 nm, A is the effective area of the device (0.023 cm^2), q is the actual charge 1.6×10^{-19} C, J^*_{ph} and J_{d} are the photocurrent and dark current (measured at a light intensity of 1 mW/cm^2), and the data obtained by equation calculation are shown in Table S1. The responsivity demonstrated in Fig. 4d, showed an increasing trend, which is attributed to the higher I^*_{ph} ($I^*_{\text{ph}} = I_{\text{photo}} - I_{\text{dark}}$) value of the device. It is found that the responsivity of the device with one $Ti_3C_2T_X$ layer (device B) shows the most apparent improvement compared to the ZnO device, about an order of magnitude higher. In addition, it is found that the device with one $Ti_3C_2T_X$ insertion layer exhibits the highest LDR value, indicating that the device can detect optical signals in a wider range of light intensity, but the LDR decreases with the further increase of $Ti_3C_2T_X$ insertion layer. D^* and NEP are essential parameters to measure the ability of PDs to receive weak signals. It found that device B with one $Ti_3C_2T_X$ layer exhibits a lower NEP value and a higher normalized detection rate, which can be seen in Figs. 4c and e. A well normalized detectability requires higher responsivity and lower dark current. The PDs with the $Ti_3C_2T_X$ exhibits elevated responsivity, noise equivalent power, and normalized detection rate, demonstrating the overall performance of the ZnO Schottky PDs can be dramatically improved by inserting $Ti_3C_2T_X$ modified layer.

In summary, we reported a simple and clever way for improving ZnO Schottky PDs by inserting $Ti_3C_2T_X$ modified layers. Attribute to the significantly improved conductivity, the increased charge transfer and the light utilization, the optimized device with ZnO/$Ti_3C_2T_X$/ZnO hybrid structure (device B, the solution concentration of $Ti_3C_2T_X$ nanosheets was 1 mg/mL), exhibits the shortest τ_{rise} of 1.5 s, the highest detection rate of 2.53×10^9 Jones and the lowest noise equivalent power of 5.99×10^{-11} W, showing the best all-around performance. The results demonstrate promising applications of ZnO/$Ti_3C_2T_X$/ZnO in UV photoswitch and image sensor fields. And provides guidance for the further development of low-cost ZnO Schottky PDs. In the meantime, we shed light on the utilization of two dimensional MXenes in the high-performance photoelectric detection application.

Declaration of competing interest

The authors declare that they have no known competing financial interests or personal relationships that could have appeared to influence the work reported in this paper.

Acknowledgments

The authors gratefully acknowledge support from Zhejiang Provincial Natural Science Foundation (No. LY19F050007), the National Natural Science Foundation of China (No. 11604298) and Zhoushan Science and Technology Project (Nos. 2019C21029, 2019C21017)

Supplementary materials

Supplementary material associated with this article can be found, in the online version, at doi:10.1016/j.cclet.2022.107881.

References

[1] N. Nasiri, R. Bo, F. Wang, et al., Adv. Mater. 27 (2015) 4336–4343.
[2] B. Ouyang, K. Zhang, Y. Yang, Adv. Mater. Technol. (2017) 1700208.
[3] S. Liu, M.Y. Li, J. Zhang, et al., Nano Micro Lett. 12 (2020) 114.
[4] Y. Cao, P. Qu, C. Wang, et al., Adv. Opt. Mater. (2022) 2200816.
[5] Z. Wei, Y. Zhao, J. Jiang, et al., Chin. Chem. Lett. 31 (2020) 3055–3064.
[6] J. Zha, M. Luo, M. Ye, et al., Adv. Funct. Mater. 32 (2022) 2111970.
[7] Z. Zhang, Q. Liao, Y. Yu, et al., Nano Energy 9 (2014) 237–244.
[8] S. Dhar, T. Majumder, P. Chakraborty, S.P. Monda, Org. Electron. 53 (2018) 101–110.
[9] S.H. Tsai, Y.C. Shen, C.Y. Huang, R.H. Horng, Appl. Surf. Sci. 496 (2019) 143670.
[10] Y. Wang, L. Zhu, Y. Feng, et al., Adv. Funct. Mater. 29 (2019) 1807111.1-1807111.7.
[11] X. Zhang, J. Shao, C. Yan, et al., Mater. Des. 207 (2021) 109850.
[12] W. Zheng, T. Bian, X. Li, et al., J. Alloy. Compd. 712 (2017) 425–430.
[13] J. Lu, C. Xu, J. Dai, et al., Nanoscale 7 (2015) 3396–3403.
[14] X. Yu, X. Yu, M. Yan, et al., Sens. Actuator. A: Phys. 312 (2020) 112163.
[15] S.M.S. Al-Khazali, H.S. Al-Salman, A. Hmood, Mater. Lett. 277 (2020) 128177.
[16] S. Noothongkaew, O. Thumthan, K.S. An, Mater. Lett. 233 (2018) 318–323.
[17] Y. Jin, J. Wang, B. Sun, et al., Nano Lett. 8 (2008) 1649–1653.
[18] X. Yu, X. Yu, J. Zhang, et al., Sol. Energy Mater. Sol. Cell. 121 (2014) 28–34.
[19] A. Kim, Y. Won, K. Woo, et al., Adv. Funct. Mater. 24 (2014) 2462–2471.
[20] X. Yu, X. Yu, J. Zhang, et al., J. Alloy. Compd. 791 (2019) 1231–1240.
[21] P. Liu, P. Xiao, M. Lu, et al., Chin. Chem. Lett. 34 (2023) 107426.
[22] S.H. Talib, Z. Lu, B. Bashir, et al., Chin. Chem. Lett. 34 (2023) 107412.
[23] Q. Zhao, Y. Jiang, Z. Duan, et al., Chem. Eng. J. 438 (2022) 135588.
[24] C. Hou, H. Yu, Chem. Eng. J. 407 (2021) 127192.
[25] H. Huang, J. Zha, S. Li, C. Tan, Chin. Chem. Lett. 33 (2022) 163–176.
[26] Z. Guo, L. Gao, Z. Xu, et al., Small 14 (2018) e1802738.
[27] K. Montazeri, M. Currie, L. Verger, et al., Adv. Mater. 31 (2019) e1903271.
[28] X. Zhao, J. Chen, C. Zhao, et al., Appl. Surf. Sci. 570 (2021) 151183.
[29] D. Wang, Y. Fang, W. Yu, et al., Sol. Energy Mater. Sol. Cell. 220 (2021) 110850.
[30] H. Lin, X. Wang, L. Yu, et al., Nano Lett. 17 (2017) 384–391.
[31] D.B. Velusamy, J.K. El-Demellawi, A.M. El-Zohry, et al., Adv. Mater. 31 (2019) e1807658.
[32] S. Kunwar, S. Pandit, J.H. Jeong, J. Lee, Nano Micro Lett. 12 (2020) 91.
[33] M.Y. Li, M. Yu, D. Su, et al., Small 15 (2019) e1901606.
[34] K. Lv, J. Hu, X. Li, M. Li, J. Mol. Catal. A Chem. 356 (2012) 78–84.
[35] L. Xu, F. Xian, G. Zheng, M. Lai, Mater. Res. Bull. 99 (2018) 144–151.
[36] Z. Wu, H. Yu, S. Shi, Y. Li, J. Mater. Chem. A 7 (2019) 14776–14789.
[37] F.H. Alsultany, Z. Hassan, N.M. Ahmed, et al., Opt. Laser Technol. 98 (2018) 344–353.
[38] X. Jin, M. Gotz, S. Wille, et al., Adv. Mater. 25 (2013) 1342–1347.
[39] Y. Wang, S. Guo, H. Luo, et al., J. Am. Chem. Soc. 142 (2020) 16001–16006.
[40] L. Yin, C. Liu, C. Ding, et al., Cell Rep. Phys. Sci. 3 (2022) 100905.
[41] J.H. Heo, F. Zhang, J.K. Park, et al., Joule 6 (2022) 1672–1688.
[42] F. Tan, M.I. Saidaminov, H. Tan, et al., Adv. Funct. Mater. 30 (2020) 2005155.
[43] J. Wang, J. Zhang, Y. Zhou, et al., Nat. Commun. 11 (2020) 177.
[44] L. Zuo, H. Guo, D.W. deQuilettes, et al., Sci. Adv. 3 (2017) e1700106.
[45] Y. Wang, T. Guo, Z. Tian, et al., Adv. Mater. (2022) e2108560.
[46] S. Liu, M.Y. Li, D. Su, et al., ACS Appl. Mater. Interfaces 10 (2018) 32516–32525.
[47] N. Aggarwal, S. Krishna, A. Sharma, et al., Adv. Electron. Mater. 3 (2017) 1700036.
[48] K. Mahmood, S.B. Park, Electron. Mater. Lett. 9 (2013) 161–170.
[49] L. Wen, Y. Chen, W. Liu, et al., Laser Photonics Rev. 11 (2017) 1700059.
[50] M. Valenti, A. Venugopal, D. Tordera, et al., ACS Photonics 4 (2017) 1146–1152.
[51] M. Kim, M. Lin, J. Son, et al., Adv. Opt. Mater. 5 (2017) 1700004.
[52] A. Paris, A. Vaccari, A. Calà Lesina, et al., Plasmonics 7 (2012) 525–534.
[53] R. Jia, D. Zhao, N. Gao, D. Liu, Sci. Rep. 7 (2017) 40483.
[54] C.H. Lin, C.W. Huang, P.H. Wang, et al., J. Taiwan Inst. Chem. Eng. 107 (2020) 72–78.
[55] N. Kedem, S. Blumstengel, F. Henneberger, et al., Phys. Chem. Chem. Phys. 16 (2014) 8310–8319.
[56] T. Schultz, N.C. Frey, K. Hantanasirisakul, et al., Chem. Mater. 31 (2019) 6590–6597.
[57] L. Dou, Y.M. Yang, J. You, et al., Nat. Commun. 5 (2014) 5404.